A third-order gas-kinetic scheme for three-dimensional inviscid and viscous flow computations ☆

Liang Pan, Kun Xu *

Department of Mathematics and Department of Mechanical and Aerospace Engineering, Hong Kong University of Science and Technology, Clear Water Bay, Kowloon, Hong Kong

ABSTRACT

With the WENO reconstruction, a third-order multidimensional gas-kinetic scheme, with inclusion of both normal and tangential derivatives of macroscopic flow variables, is constructed for the three-dimensional inviscid and viscous flow computations. For the flux evaluation, a time and space dependent gas distribution function from an initial piece-wise discontinuous polynomials around a cell interface is presented, where a multiple scale physical process from the kinetic to the hydrodynamic one is used for the flow evolution process. A high-order accuracy is achieved in the current scheme by integrating the space and time dependent flux function over the surface of a cell interface and a whole time step, without using the conventional Gaussian points integration for spatial accuracy and Runge–Kutta method for temporal accuracy, which have been used in many other high-order schemes. This scheme is applied to both inviscid and viscous, and low and high speed flow computations. The numerical tests clearly demonstrate that the current scheme is robust for the flows with strong discontinuities and accurate for viscous smooth flow solutions. The continuous effort on the gas kinetic scheme (GKS) is to develop a third method which has the same reliability and robustness as the well-developed second-order shock capturing schemes, but is simply much more accurate in all flow applications. The current scheme seems achieve such a target.

© 2015 Elsevier Ltd. All rights reserved.

1. Introduction

In the field of computational fluid dynamics, low-order methods are generally robust and reliable. As a result, they are routinely employed in the practical calculations. For the same computational cost, high-order methods can provide more accurate solutions, but they are less robust and more complicated. In recent years, many high-order numerical methods have been developed for the Euler and Navier–Stokes equations, including discontinuous Galerkin (DG), spectral volume (SV), spectral difference (SD), correction procedure using reconstruction (CPR), essential non-oscillatory (ENO), weighted essential non-oscillatory (WENO) and $P_N P_M$ schemes, etc. The DG scheme was first proposed [32] to solve the neutron transport equation. The major development of DG method was carried out for the compressible Euler equations [7,8] and the Navier–Stokes equations [9,27]. In the DG method, high-order accuracy is achieved by means of high-order polynomial approximation within each element rather than by means of wide stencils. Because only neighboring elements interaction is included, it

becomes efficient in the application of complex geometry. Explicit Runge–Kutta method is used for the time discretization, which makes the algorithm highly parallel. Recently, a correction procedure via reconstruction framework (CPR) was developed [16,40]. This method was originally developed for the one-dimensional conservation laws, under the name of flux reconstruction (FR) [19,20]. Under the lifting collocation penalty, the CPR framework was extended to two-dimensional triangular and mixed grids. The CPR formulation is based on a nodal differential form, with an element-wise continuous polynomial solution space. By choosing certain correction functions, the CPR framework can unify several well known methods, such as the DG, SV [26], and SD [39] methods, and lead to simplified versions of these methods, at least for linear equations. The ENO scheme was proposed in [18,36] and successfully applied to solve hyperbolic conservation laws and other convection dominated problems. Following the ENO scheme, WENO scheme [25,22,21] was further developed. ENO scheme uses the smoothest stencil among several candidates to approximate the numerical fluxes at cell interface for high-order accuracy. At the same time, it avoids spurious oscillations near discontinuities. Meanwhile, WENO scheme is a convex linear combination of lower order reconstructions to obtain a higher order approximation. WENO scheme improves upon ENO scheme in

---

robustness, smoothness of fluxes, steady-state convergence, provable convergence properties, and more efficiency. Based on the WENO reconstruction, the high order three-dimensional schemes for compressible flows were also developed [15,37,38]. In most ENO and WENO schemes, large stencils in the high-order reconstruction and Runge–Kutta time stepping are used, especially for the multi-dimensional unstructured meshes [22]. Certainly, some schemes use Cauchy–Kowalewski procedure, such as the ADER formulation [38,15], but the evolution equations for higher order derivatives are based on the linearized equations and it is also unclear how to incorporate the viscous and heat conduction terms in the higher order equations. The $P_N P_M$ scheme is family of numerical methods proposed for the Euler and Navier–Stokes equations [13,14], where N indicates the polynomial degree of the test functions and M is the degree of the polynomials used for flux and source computation. This approach yields a general, unified framework that contains two special cases, i.e. the classical high order finite volume scheme ($N = 0$) as well as the DG method ($N = M$).

The gas-kinetic scheme (GKS) based on the Bhatnagar–Gross–Krook (BGK) model [2,4,5] has been developed systematically for the compressible flow computations [41–43]. The gas-kinetic scheme presents a gas evolution process from a kinetic scale to a hydrodynamic scale, where both inviscid and viscous fluxes are recovered from the moments of a single time-dependent gas distribution function. In discontinuous shock region, the kinetic scale physics, such as particle free transport, takes effect to construct a crisp and stable shock transition. The highly non-equilibrium of the gas distribution function in the discontinuous region provides a physically consistent mechanism for the construction of numerical shock structure. In smooth flow region, the hydrodynamic scale physics corresponding to the multi-dimensional central difference discretization will contribute mainly in the kinetic flux function, and accurate Navier–Stokes solution can be obtained once the flow structure is well resolved. With the discretization of particle velocity space, a unified gas-kinetic scheme (UGKS) has been developed for the flow study in entire Knudsen number regimes from rarefied to continuum ones [44,29,43]. Recently, with the incorporation of high-order initial reconstruction, high-order gas-kinetic schemes have been constructed [24,28,30]. The flux evaluation in the scheme is based on the moments of a time and space dependent gas distribution function evolved from an initially piece-wise discontinuous polynomials of macroscopic flow variables around a cell interface, where high-order spatial and temporal derivatives of flow variables are coupled nonlinearly. The whole curves of discontinuous flow distributions around a cell interface interact through particle transport and collision in the determination of the flux function. Therefore, the use of the space and time dependent flux function including both inviscid and viscous terms in the current scheme distinguishes it from any other high-order scheme with the Riemann solver, or the schemes with linearized evolution equations for high-orders flow variable derivatives.

In this paper, with the WENO reconstruction, a high-order gas-kinetic scheme is developed for the three-dimensional Euler and Navier–Stokes equations. It is a multidimensional method, in which both normal and tangential derivatives of macroscopic flow variables are included in the determination of local solution. The numerical fluxes are obtained by taking moments of the time and space dependent gas distribution function and the fluxes are integrated over the surface of a cell interface and the whole time step for the evaluation of total flow transport across a cell boundary. Therefore, the Gaussian point integration for spatial accuracy and Runge–Kutta method for time accuracy are not needed in the current scheme. Numerical test cases for inviscid and viscous flows are used to validate the current scheme.

This paper is organized as follows. In Section 2, the BGK model and the finite volume scheme are introduced. In Section 3, a high-order gas-kinetic scheme and reconstruction techniques for the macroscopic flow variables are presented. Section 4 includes numerical examples to validate the current algorithm. The last section is the conclusion.

2. Gas-kinetic equation and finite volume scheme

The three-dimensional BGK equation can be written as

$$f_t + uf_x + vf_y + wf_z = \frac{g - f}{\tau}, \tag{1}$$

where f is the gas distribution function, g is the corresponding equilibrium state and τ is the collision time. The collision term satisfies the compatibility condition

$$\int \frac{g - f}{\tau} \psi d\Xi = 0, \tag{2}$$

where $\psi = (1, u, v, w, \frac{1}{2}(u^2 + v^2 + w^2 + \xi^2))$, the internal variables ξ^2 is equal to $\xi^2 = \xi_1^2 + \ldots + \xi_K^2, d\Xi = dudvdwd\xi_1 \ldots d\xi_K, K$ is the degrees of freedom, i.e. $K = (5 - 3\gamma)/(\gamma - 1)$ for three-dimensional flows, and γ is the specific heat ratio.

Based on the Chapman–Enskog expansion of the BGK model, the Euler, Navier–Stokes, Burnett, and Super-Burnett equations can be derived [5,41]. In the smooth region, the gas distribution function can be expanded as

$$f = g - \tau D_{\mathbf{u}} g + \tau D_{\mathbf{u}}(\tau D_{\mathbf{u}})g - \tau D_{\mathbf{u}}[\tau D_{\mathbf{u}}(\tau D_{\mathbf{u}})g] + \cdots,$$

where $D_{\mathbf{u}} = \frac{\partial}{\partial t} + \mathbf{u} \cdot \nabla$. By truncating different orders of τ, the corresponding macroscopic equations can be derived. For the Euler equations, the zeroth order truncation is taken, i.e. $f = g$. For the Navier–Stokes equations, the first order truncation is

$$f = g - \tau(ug_x + vg_y + wg_z + g_t). \tag{3}$$

With the higher order truncations, the Burnett and super-Burnett equations can be derived.

In the gas-kinetic scheme, the numerical fluxes in the x direction can be obtained by taking moments of the gas distribution function

$$F_{i+1/2,j,k} = \int \psi u f(x_{i+1/2}, y, z, t, u, v, w, \xi) d\Xi,$$

where $f(x_{i+1/2}, y, z, t, u, v, w, \xi)$ is the gas distribution function at the cell interface, and will be introduced in the following section. Similarly, the numerical fluxes $G_{i,j+1/2,k}$ and $H_{i,j,k+1/2}$ in the y and z directions can be also obtained. With these numerical fluxes, the finite volume scheme can be obtained by taking moments of the BGK Eq. (1) and integrating with respect to time and space

$$
\begin{aligned}
W_{ijk}^{n+1} = W_{ijk}^{n} + \frac{1}{\Delta x \Delta y \Delta z} \int_{t^n}^{t^{n+1}} &\left[\int_{\bar{y}_j \times \bar{z}_k} (F_{i-1/2,j,k} - F_{i+1/2,j,k}) dydz \right. \\
&+ \int_{\bar{x}_i \times \bar{z}_k} (G_{i,j-1/2,k} - G_{i,j+1/2,k}) dxdz \\
&\left. + \int_{\bar{x}_i \times \bar{y}_j} (H_{i,j,k-1/2} - H_{i,j,k+1/2}) dxdy \right] dt,
\end{aligned} \tag{4}
$$

where $\bar{x}_i = [x_i - \Delta x/2, x_i + \Delta x/2], \bar{y}_j = [y_j - \Delta y/2, y_j + \Delta y/2], \bar{z}_k = [z_k - \Delta z/2, z_k + \Delta z/2]$ and $W = (\rho, \rho U, \rho V, \rho W, \rho E)$ are the conservative flow variables.

3. High-order GKS and reconstruction

3.1. High-order GKS

In this section, a multidimensional high-order gas-kinetic solver will be presented based on the high-order initial reconstruction which will be given in the next subsection. To construct the numerical fluxes, the integral solution of Eq. (1) at the cell interface is

$$f(x_{i+1/2}, y, z, t, u, v, w, \xi) = \frac{1}{\tau} \int_0^t g(x', y', z', t', u, v, w, \xi) e^{-(t-t')/\tau} dt'$$
$$+ e^{-t/\tau} f_0(-ut, y - vt, z - wt, \xi), \quad (5)$$

where $x_{i+1/2} = 0$ is the location of cell interface, $x_{i+1/2} = x' + u(t - t'), y = y' + v(t - t')$ and $z = z' + w(t - t')$ are the trajectory of particle. Based on the macroscopic reconstruction given in the next subsection, the gas distribution function can be fully determined.

Remark 1. In the above integral solution, the initial term f_0 accounts for particle free transport, which represents the kinetic scale physics. The integration of equilibrium state along the particle trajectory represents the accumulating effect of an equilibrium state, which is related to the hydrodynamic scale physics. The flow behavior at cell interface depends on the ratio of time step and local particle collision time $\Delta t/\tau$. The Navier-Stokes solutions will be the limiting solutions of the GKS underlying the assumption of near equilibrium state in the initial condition and the flow structure is well resolved by the mesh size scale.

To construct the flow solver, the following notations are introduced

the notation for future presentation, $\langle \ldots \rangle$ are defined as the moments of gas distribution function

$$\langle \ldots \rangle = \int g(\ldots) \psi d\Xi,$$

where g is the corresponding equilibrium state.

For the flow with discontinuity at a cell interface, with the reconstructed polynomial on both sides of the interface, the initial Navier–Stokes gas distribution function can be constructed as

$$f_0 = f_0^l(x, y, z, u, v, w, \xi)H(x) + f_0^r(x, y, z, u, v, w, \xi)(1 - H(x)), \quad (6)$$

where $H(x)$ is the Heaviside function, f_0^l and f_0^r are the initial gas distribution functions on both sides of the cell interface, which have one to one correspondence with the initially reconstructed polynomials of macroscopic flow variables. To third-order accuracy, the Taylor expansion for the gas distribution function in space at $(x, y, z) = (0, 0, 0)$ is expressed as

$$f_0^k(x, y, z) = f_G^k(0, 0, 0) + \frac{\partial f_G^k}{\partial x} x + \frac{\partial f_G^k}{\partial y} y + \frac{\partial f_G^k}{\partial z} z + \frac{1}{2} \frac{\partial^2 f_G^k}{\partial x^2} x^2 + \frac{1}{2} \frac{\partial^2 f_G^k}{\partial y^2} y^2$$
$$+ \frac{1}{2} \frac{\partial^2 f_G^k}{\partial z^2} z^2 + \frac{\partial^2 f_G^k}{\partial x \partial y} xy + \frac{\partial^2 f_G^k}{\partial x \partial z} xz + \frac{\partial^2 f_G^k}{\partial y \partial z} yz,$$

where $k = l, r$. For the inviscid flow, the initial gas distribution function takes $f_G^k = g_k$. For the viscous flow, according to (3), it takes $f_G^k = g_k(1 - \tau(a_{1k}u + a_{2k}v + a_{3k}w + A_k))$, and the corresponding kinetic part of (5) can be written as

$$e^{-t/\tau} f_0^k(-ut, y - vt, z - wt, u, v, w, \xi) = C_7 g_k [1 - \tau(a_{1k}u + a_{2k}v + a_{3k}w + A_k)]$$
$$+ C_8 g_k [a_{1k}u - \tau((a_{1k}^2 + d_{11k})u^2 + (a_{1k}a_{2k} + d_{12k})uv + (a_{1k}a_{3k} + d_{13k})uw + (A_k a_{1k} + b_{1k})u)]$$
$$+ C_8 g_k [a_{2k}v - \tau((a_{1k}a_{2k} + d_{12k})uv + (a_{2k}^2 + d_{22k})v^2 + (a_{2k}a_{3k} + d_{23k})vw + (A_k a_{2k} + b_{2k})v)]$$
$$+ C_8 g_k [a_{3k}w - \tau((a_{1k}a_{3k} + d_{13k})uw + (a_{2k}a_{3k} + d_{23k})vw + (a_{3k}^2 + d_{33k})w^2 + (A_k a_{3k} + b_{3k})w)]$$
$$+ C_7 g_k [a_{2k} - \tau((a_{1k}a_{2k} + d_{12k})u + (a_{2k}^2 + d_{22k})v + (a_{2k}a_{3k} + d_{23k})w + (A_k a_{2k} + b_{2k}))]y$$
$$+ C_7 g_k [a_{3k} - \tau((a_{1k}a_{3k} + d_{13k})u + (a_{2k}a_{3k} + d_{23k})w + (a_{3k}^2 + d_{33k})v + (A_k a_{3k} + b_{3k}))]z$$
$$+ \frac{1}{2} C_7 [g_k(a_{1k}^2 + d_{11k})(-ut)^2 + (a_{2k}^2 + d_{22k})(y - vt)^2 + (a_{2k}^2 + d_{22k})(z - wt)^2] + C_7 g_k[(a_{1k}a_{2k} + d_{12k})(-ut)(y - vt) + (a_{1k}a_{3k} + d_{13k})(-ut)(z - wt)], + C_7 g_k(a_{2k}a_{3k} + d_{23k})(y - vt)(z - wt), \quad (7)$$

$$a_1 = (\partial g/\partial x)/g, a_2 = (\partial g/\partial y)/g, a_3 = (\partial g/\partial z)/g,$$
$$A = (\partial g/\partial t)/g, B = (\partial A/\partial t), d_{11} = (\partial a_1/\partial x), d_{22} = (\partial a_2/\partial y),$$
$$d_{33} = (\partial a_3/\partial z),$$
$$d_{12} = (\partial a_1/\partial y) = (\partial a_2/\partial x), d_{13} = (\partial a_1/\partial z) = (\partial a_3/\partial x),$$
$$d_{23} = (\partial a_3/\partial y) = (\partial a_2/\partial z),$$
$$b_1 = (\partial a_1/\partial t) = (\partial A/\partial x), b_2 = (\partial a_2/\partial t) = (\partial A/\partial y),$$
$$b_3 = (\partial a_3/\partial t) = (\partial A/\partial z).$$

The dependence of the coefficients on particle velocity is expanded as

$$a_1 = a_{11} + a_{12}u + a_{13}v + a_{14}w + a_{15} \frac{1}{2}(u^2 + v^2 + w^2 + \xi^2),$$

$$\cdots$$

$$B = B_1 + B_2 u + B_3 v + B_4 w + B_5 \frac{1}{2}(u^2 + v^2 + w^2 + \xi^2),$$

where $a_{11}, \ldots, a_{15}, B_1, \ldots, B_5$ are local constants. All above coefficients will be fully determined from macroscopic flow variables, which are the moments of the equilibrium state. In order to simplify

where g_k are the equilibrium states at both sides of the cell interface, and the coefficients $a_{1k}, \ldots, A_k$ are defined according to the expansion of g_k.

After determining the kinetic part f_0, the equilibrium state g in the integral solution (5) can be constructed consistently with f_0 as follows

$$g = g_0 + \frac{\partial g_0}{\partial x} x + \frac{\partial g_0}{\partial y} y + \frac{\partial g_0}{\partial z} z + \frac{\partial g_0}{\partial t} t + \frac{1}{2} \frac{\partial^2 g_0}{\partial x^2} x^2 + \frac{1}{2} \frac{\partial^2 g_0}{\partial y^2} y^2$$
$$+ \frac{1}{2} \frac{\partial^2 g_0}{\partial z^2} z^2 + \frac{1}{2} \frac{\partial^2 g_0}{\partial t^2} t^2 + \frac{\partial^2 g_0}{\partial x \partial y} xy + \frac{\partial^2 g_0}{\partial x \partial z} xz + \frac{\partial^2 g_0}{\partial y \partial z} yz$$
$$+ \frac{\partial^2 g_0}{\partial x \partial t} xt + \frac{\partial^2 g_0}{\partial y \partial t} yt + \frac{\partial^2 g_0}{\partial z \partial t} zt, \quad (8)$$

where g_0 is the equilibrium state located at the interface, which can be determined through the compatibility condition (2)

$$\iint \psi g_0 d\Xi = W_0 = \iint_{u>0} \psi g_l d\Xi + \iint_{u<0} \psi g_r d\Xi, \quad (9)$$

where g_l, g_r are the equilibrium states at both sides of the cell inter-face. Based on the Taylor expansion for equilibrium state (8), the hydrodynamic part in (5) can be written as

$$
\begin{aligned}
\frac{1}{\tau} \int_0^t & g(x', y', z', t', u, v, w, \xi) e^{-(t-t')/\tau} dt' \\
&= C_1 g_0 + C_2 g_0 \bar{a}_1 u + C_2 g_0 \bar{a}_2 v + C_2 g_0 \bar{a}_3 w + C_3 g_0 \bar{A} \\
&+ \frac{1}{2} C_4 \left[g_0 (\bar{a}_1^2 + \bar{d}_{11}) u^2 + (\bar{a}_2^2 + \bar{d}_{22}) v^2 + (\bar{a}_3^2 + \bar{d}_{33}) w^2 \right] \\
&+ C_4 g_0 [(\bar{a}_1 \bar{a}_2 + \bar{d}_{12}) uv + (\bar{a}_2 \bar{a}_3 + \bar{d}_{23}) vw + (\bar{a}_1 \bar{a}_3 + \bar{d}_{13}) uw] \\
&+ C_6 g_0 [(\bar{A} \bar{a}_1 + \bar{b}_1) u + (\bar{A} \bar{a}_2 + \bar{b}_2) v + (\bar{A} \bar{a}_3 + \bar{b}_2) w] \\
&+ \frac{1}{2} g_0 \left[C_1 (\bar{a}_2^2 + \bar{d}_{22}) y^2 + C_1 (\bar{a}_3^2 + \bar{d}_{33}) z^2 + C_5 (\bar{A}^2 + \bar{B}) \right], \quad (10)
\end{aligned}
$$

where the coefficients $\bar{a}_1, \bar{a}_2, \ldots, \bar{A}, \bar{B}$ are defined from the expansion of the equilibrium state g_0. The coefficients $C_i, i = 1, \ldots, 8$ in (10) and (7) are given by

$$C_1 = 1 - e^{-t/\tau}, C_2 = (t + \tau) e^{-t/\tau} - \tau, C_3 = t - \tau + \tau e^{-t/\tau},$$
$$C_4 = -(t^2 + 2t\tau) e^{-t/\tau},$$
$$C_5 = t^2 - 2t\tau, C_6 = -t\tau(1 + e^{-t/\tau}), C_7 = e^{-t/\tau}, C_8 = -te^{-t/\tau}.$$

The linear terms with respect to y and z are omitted for simplic-ity, because their integrations are zero in (4). Substituting (10) and (7) into the integral solution (5), the gas distribution function at the cell interface can be fully determined. With the gas distribution function (5), the numerical fluxes can be obtained by taking moments of it and integrating with respect to time and space.

For smooth flow, the reconstructed polynomials at both sides of cell interface will take the same form $\overline{W}(x)$, which is continuous $g_0 = g_l = g_r$ and has identical slope. Consequently, the gas distribu-tion function (5) will reduce to a continuous one

$$
\begin{aligned}
f = g_0 & [1 - \tau(\bar{a}_1 u + \bar{a}_2 v + \bar{a}_3 w + \bar{A})] \\
&+ g_0 \left[\bar{A} - \tau((\bar{A}\bar{a}_1 + \bar{b}_1) u + (\bar{A}\bar{a}_2 + \bar{b}_2) v + (\bar{A}\bar{a}_3 + \bar{b}_3) v + (\bar{A}^2 + \bar{B})) \right] t \\
&+ g_0 \left[\frac{1}{2} (\bar{a}_2^2 + \bar{d}_{22}) y^2 + \frac{1}{2} (\bar{a}_3^2 + \bar{d}_{33}) z^2 + \frac{1}{2} (\bar{A}^2 + \bar{B}) t^2 \right],
\end{aligned}
$$

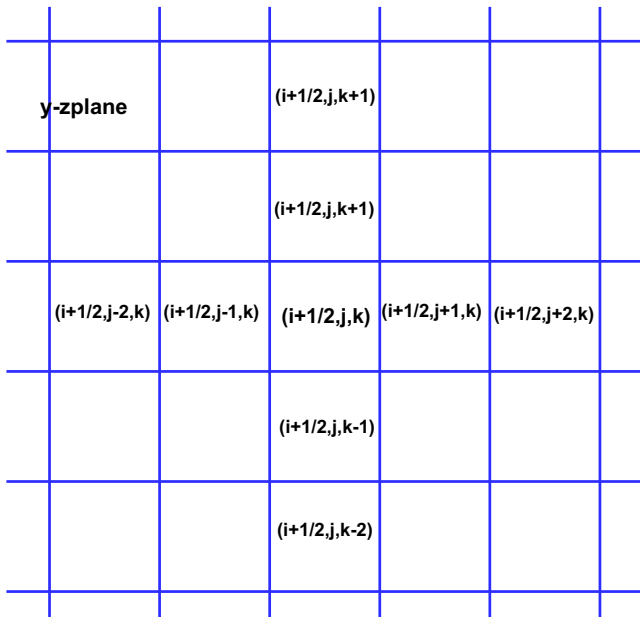where the linear terms with respect to y and z are also omitted for simplicity.

Fig. 1. Schematics of construction of derivatives at the cell interface $x_{i+1/2} = 0$.

All coefficients in (10) and (7) can be determined by the spatial derivatives of macroscopic flow variables and their connection with the moments of a gas distribution function,

$$
\begin{cases}
\langle a_1 \rangle = \frac{\partial W}{\partial x}, \langle a_2 \rangle = \frac{\partial W}{\partial y}, \langle a_3 \rangle = \frac{\partial W}{\partial z}, \langle A + a_1 u + a_2 v + a_3 w \rangle = 0, \\
\langle a_1^2 + d_{11} \rangle = \frac{\partial^2 W}{\partial x^2}, \langle a_2^2 + d_{22} \rangle = \frac{\partial^2 W}{\partial y^2}, \langle a_3^2 + d_{33} \rangle = \frac{\partial^2 W}{\partial z^2}, \\
\langle a_1 a_2 + d_{12} \rangle = \frac{\partial^2 W}{\partial x \partial y}, \langle a_1 a_3 + d_{13} \rangle = \frac{\partial^2 W}{\partial x \partial z}, \langle a_2 a_3 + d_{23} \rangle = \frac{\partial^2 W}{\partial y \partial z}, \\
\langle (a_1^2 + d_{11}) u + (a_1 a_2 + d_{12}) v + (a_1 a_3 + d_{13}) w + (Aa_1 + b_1) \rangle = 0, \\
\langle (a_2 a_1 + d_{21}) u + (a_2^2 + d_{22}) v + (a_2 a_3 + d_{23}) w + (Aa_2 + b_2) \rangle = 0, \\
\langle (a_3 a_1 + d_{31}) u + (a_3 a_2 + d_{32}) v + (a_3^2 + d_{33}) w + (Aa_3 + b_3) \rangle = 0, \\
\langle (Aa_1 + b_1) u + (Aa_2 + b_2) v + (Aa_3 + b_3) w + (A^2 + B) \rangle = 0,
\end{cases} \tag{11}
$$

where the superscripts or subscripts of these coefficients $a_1, \ldots, A, B$ are omitted for simplicity, and more details about the determina-tion of coefficients can be found in [42]. The reconstruction of the derivatives of macroscopic flow variables will be given in the next subsection.

Remark 2. Because of the multi-dimensionality, the numerical evaluation of (5) becomes very tedious. However, in the conven-tional high-order schemes, the Gaussian points integration and the Runge–Kutta method are used, where many more numerical fluxes

Table 1
Space accuracy test for the isotropic vortex propagation problem.

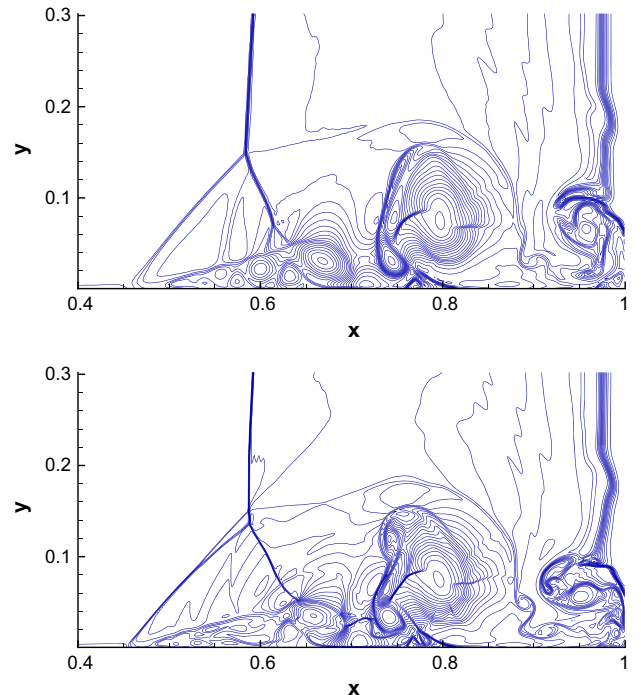| Grid	L^1 norm	Order	L^2 norm	Order
21 × 21	3.31446E−02		6.32088E−02	
41 × 41	5.61167E−03	2.562271	9.57611E−03	2.722613
81 × 81	8.84818E−04	2.664978	1.54468E−03	2.632132
161 × 161	1.16459E−04	2.925551	2.15638E−04	2.840623
321 × 321	1.63067E−05	2.836286	3.11221E−05	2.792601

Fig. 2. Reflected shock-boundary layer interaction: the density distribution at $t = 1$ with 500×250 and 1000×500 (from top to bottom) mesh points at $Re = 1000$.
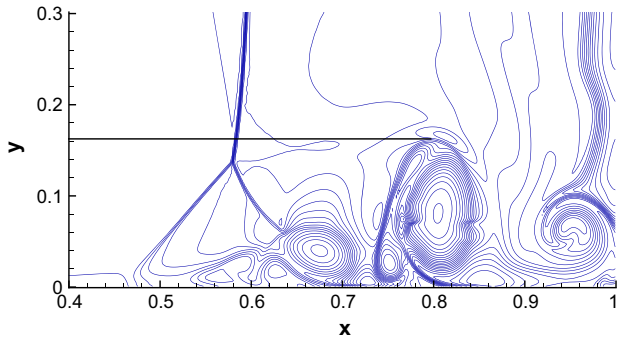
Fig. 3. Reflected shock-boundary layer interaction: the density distribution at $t = 1$ with 500×250 mesh points with $Re = 200$.

Table 2
Comparison of the height of primary vortex with 500×250 mesh points for the reflected shock-boundary layer interaction at $Re = 200$.

Scheme	AUSMPW+ [23]	M-AUSMPW+ [23]	current
height	0.163	0.166	0.1625

are evaluated within a time step. In comparison with the conventional high-order schemes, the computational cost of current scheme is still reasonable.

3.2. Reconstruction

The above time evolution solution is based on the high-order initial reconstruction of macroscopic flow variables. For the initial reconstruction, the WENO scheme [22] is adopted. In the following sections, with no special statement, for the smooth flow, the third-order reconstruction is used for the conservative flow variables; for the flow with discontinuity, fifth-order reconstruction is used for the characteristic variables.

To construct the initial distribution f_0, the corresponding polynomials in the normal direction are obtained as follows. With the cell averaged value W_i and the reconstructed variables at two ends of each cell W_i^r and W_i^l, a third-order polynomial inside each cell can be expressed as

$$W_i(x) = W_i + \left(\frac{\partial W}{\partial x}\right)_i (x - x_i) + \frac{1}{2}\left(\frac{\partial^2 W}{\partial x^2}\right)_i \left[(x - x_i)^2 - \frac{1}{12}\Delta x^2\right],$$

where $x \in [x_{i-1/2}, x_{i+1/2}]$. The first and second order normal derivatives at both sides of the cell interface can be determined from this polynomial. The stencil for the tangential derivatives are shown in
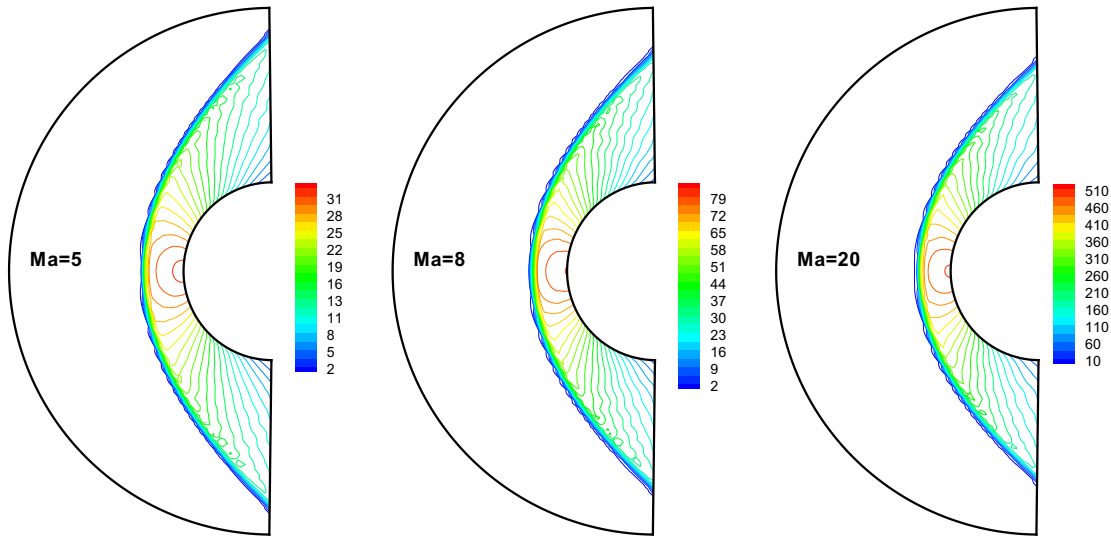

Fig. 4. The pressure distribution for the flow impinging on a cylinder at $Ma = 5, 8$ and 20.
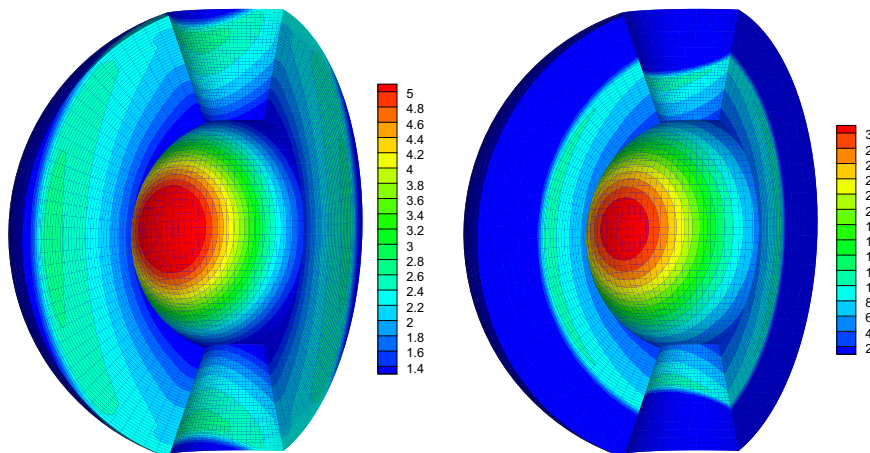

Fig. 5. The pressure distribution for the flow impinging on a sphere at $Ma = 2$ and 5 (from left to right).

Fig. 1. Based on the reconstructed data $W^r_{i,j-m,k}, W^l_{i+1,j-m,k}$ and $W^r_{i,j,k-m}, W^l_{i+1,j,k-m}, m = -2, \ldots, 2$, the first and second order tangential terms can be also obtained on both sides of cell interface. The cross derivatives $\frac{\partial^2 W}{\partial x \partial y}, \frac{\partial^2 W}{\partial x \partial z}$ and $\frac{\partial^2 W}{\partial y \partial z}$ can be obtained by the finite difference of the conservative variables at both sides of the cell interface $(i + 1/2, j, k)$. For the smooth flow, the central difference discretization is adopted; for the flow with discontinuity, the technique of nonlinear weight is used to improve the robustness of reconstruction. With the reconstructed polynomials and derivatives on both sides of the cell interface, the coefficients $a_{1k}, a_{2k}, \ldots, A_k, k = l, r$ in (7) can be determined according to (11).

To determine the equilibrium state g across the cell interface, the conservative variables around the cell interface in the normal direction can be expanded as

$$\overline{W}(x) = W_0 + S_i^1(x - x_i) + \frac{1}{2}S_i^2(x - x_i)^2 + \frac{1}{6}S_i^3(x - x_i)^3 + \frac{1}{24}S_i^4(x - x_i)^4,$$

where W_0 are the conservative flow variables corresponding to the equilibrium state g_0 at the cell interface obtained from the compatibility condition (9). With the following conditions

$$\frac{1}{(\Delta x)_{i+k}} \int_{l_{i+k}} \overline{W}(x)dx = W_{i+k}, \ k = -1, \ldots, 2,$$

the polynomial $\overline{W}(x)$ can be fully determined. Similarly, the tangential and cross derivatives can be constructed across the cell interface. With the polynomials $\overline{W}(x)$ across the cell interface, the
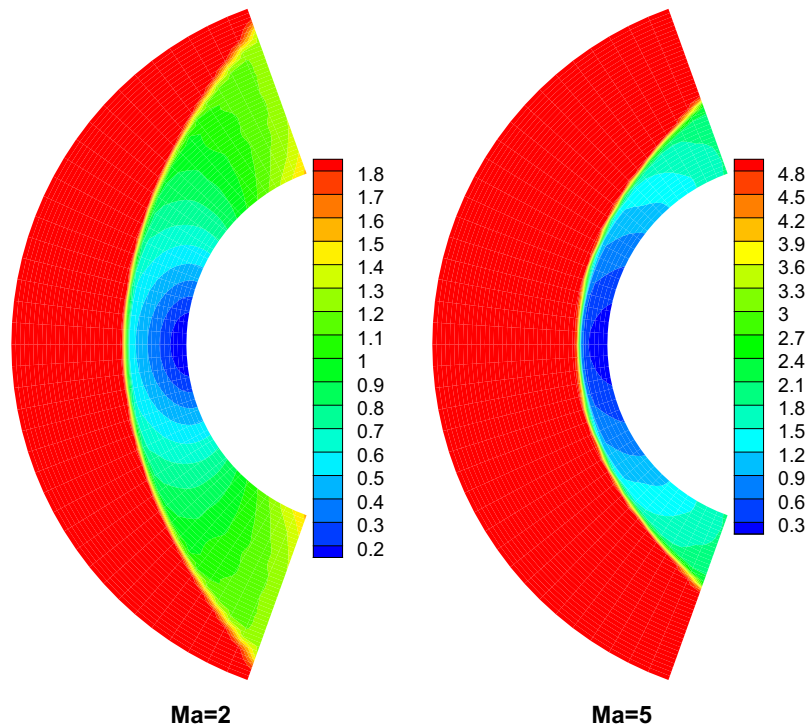

Ma=2   **Ma=5**

Fig. 6. The Mach number distributions at the symmetric $r - \theta$ plane with $\phi = 0$ for the flow impinging on a sphere at $Ma = 2$ and 5.
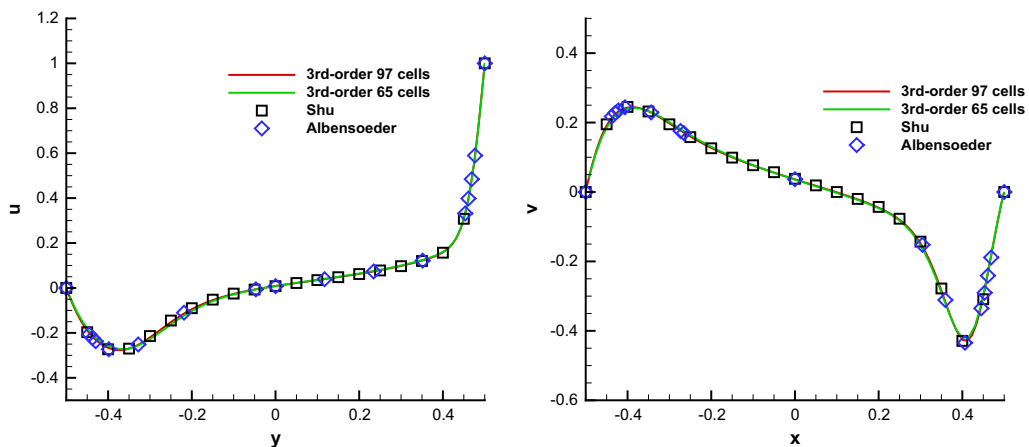

Fig. 7. 3D cavity flow: the profiles of U-velocity along the vertical centerline line and V-velocity along the horizontal centerline at the xy-plane with $z = 0$ with $Re = 1000$, where the reference data is from Albensoeder [1] and Shu [34] using $65 \times 65 \times 65$ and $97 \times 97 \times 97$ mesh points.

derivatives of $\overline{W}(x)$ can be calculated and the coefficients $\overline{a}_1, \overline{a}_2, \ldots, \overline{A}, \overline{B}$ in (10) are determined according to (11).

4. Numerical tests

In this section, numerical tests for both inviscid and viscous flows will be presented to validate the numerical scheme. For the inviscid flow, the collision time τ takes

$$\tau = \varepsilon \Delta t + C \left| \frac{p_l - p_r}{p_l + p_r} \right| \Delta t. \tag{12}$$

In the computation, $\varepsilon = 0.01$ and $C = 1$. For the viscous flow, we have

$$\tau = \frac{\mu}{p} + \left| \frac{p_l - p_r}{p_l + p_r} \right| \Delta t,$$

where p_l and p_r denote the pressure on the left and right sides of the cell interface, μ is the viscous coefficient and p is the pressure at the cell interface. In the smooth flow regions, it will reduce to $\tau = \mu/p$. For diatomic molecules with $\gamma = 1.4$, the current gas-kinetic scheme solves the Navier–Stokes equations with the inclusion of bulk viscosity. For monatomic gas with $\gamma = 5/3$, there is no bulk viscosity involved. Δt is the time step which is determined according to the CFL condition. In the numerical tests, CFL number takes values from 0.15 to 0.2.

4.1. Accuracy test

In this case, the isotropic vortex propagation problem [35] is presented to validate the accuracy for the inviscid flow. The mean flow is $(\rho, u, v, w, p) = (1, 1, 1, 0, 1)$ and an isotropic vortex is added to the mean flow, i.e. with perturbation in u, v and temperature $T = p/\rho$, and no perturbation in w and entropy $S = p/\rho^\gamma$. The initial condition is given by

$$(\delta u, \delta v, \delta w) = \frac{\epsilon}{2\pi} e^{\frac{(1-r^2)}{2}} (-y, x, 0),$$

$$\delta T = -\frac{(\gamma - 1)\epsilon^2}{8\gamma\pi^2} e^{1-r^2}, \delta S = 0,$$

where $r^2 = x^2 + y^2$ and the vortex strength $\epsilon = 5$. The exact solution is the initial condition propagating with the velocity $(1, 1, 0)$. The computational domain is $[-5, 5] \times [-5, 5] \times [0, 0.1]$, with the periodic boundary conditions imposed on all boundaries. The L^1 and L^2 errors and orders after one time period with $t = 10$ are presented in Table 1, which shows that a third-order accuracy can be achieved.

4.2. Reflecting shock-boundary layer interaction

This problem was introduced to test the performances of different schemes for viscous flow with discontinuity [10,33]. In this case, an ideal gas is at rest in a two-dimensional unit box $[0, 1] \times [0, 1]$. A membrane located at $x = 0.5$ separates two different states of the gas and the dimensionless initial states are
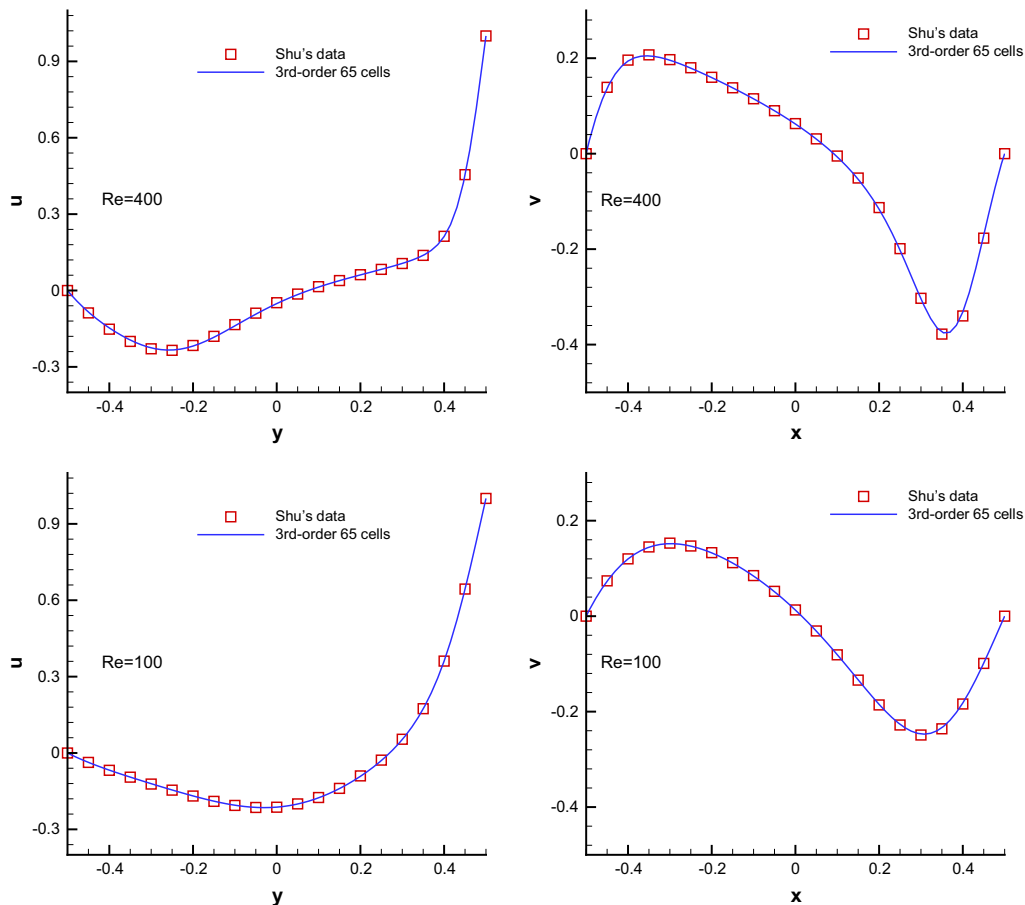

Fig. 8. 3D cavity flow: the profiles of U-velocity along the vertical centerline line and V-velocity along the horizontal centerline at the xy-plane with $z = 0$ at $Re = 400$ and 100, where the reference data is from Shu [34] using $65 \times 65 \times 65$ mesh points.

$$(\rho, u, p) = \begin{cases} (120, 0, 120/\gamma), 0 < x < 0.5, \\ (1.2, 0, 1.2/\gamma), 0.5 < x < 1, \end{cases}$$

where $\gamma = 1.4$ and Prandtl number $Pr = 0.73$.

The flow in the box $[0, 1] \times [0, 1]$ is symmetrical in y-direction, so it is tested in the half domain $[0, 1] \times [0, 0.5]$ with the implementation of a symmetrical boundary condition on the top boundary $x \in [0, 1], y = 0.5$. Non-slip boundary condition for velocity and adiabatic condition for temperature are imposed at solid walls and one cell is used in the z direction. When the membrane is removed, a shock wave, followed by a contact discontinuity, moves to the right and reflects at the right end wall. After reflection, it interacts with the contact discontinuity. The contact discontinuity and shock wave interact above the non-slip horizontal wall and create a thin boundary layer during their propagation. The solution will develop complex two-dimensional shock/shear/boundary-layer interactions. The density distributions with Reynolds number $Re = 1000$ and 200 at $t = 1$ with 500×250 and 1000×500 mesh points are shown in Figs. 2 and 3, respectively. The current scheme can well resolve the flow structure. As shown in Table 2, the height

of primary vortex predicted by the current scheme agrees well with the reference value at $Re = 200$ [23].

4.3. Flow impinging on blunt bodies

In this case, the inviscid hypersonic flows impinging on a unit cylinder and sphere are tested to validate robustness of the current scheme for different Mach numbers with $\gamma = 1.4$. For the flow impinging on cylinder, a fan-shaped domain with $81 \times 81 \times 10$ mesh points are adopted, which cover the domain $[-3, -1] \times [-\pi/2, \pi/2] \times [0, 0.2]$ in the cylindrical coordinate (r, ϕ, h). The distributions of pressure at the $r - \phi$ plane at $h = 0$ are shown in Fig. 4 for Mach numbers $Ma = 5, 8$ and 20, which show that the current scheme can capture the flow structure nicely in front of the cylinder and the carbuncle phenomenon does not appear [31]. For flow impinging on the sphere, $40 \times 40 \times 40$ mesh points are used, which cover the domain $[-2.5, -1] \times [-0.4\pi, 0.4\pi] \times [0.15\pi, 0.85\pi]$ in the spherical coordinate (r, ϕ, θ). The pressure distributions and the Mach number distributions at the symmetric $r - \theta$ plane with $\phi = 0$ are shown in Figs. 5 and 6 at Mach numbers $Ma = 2$ and 5.
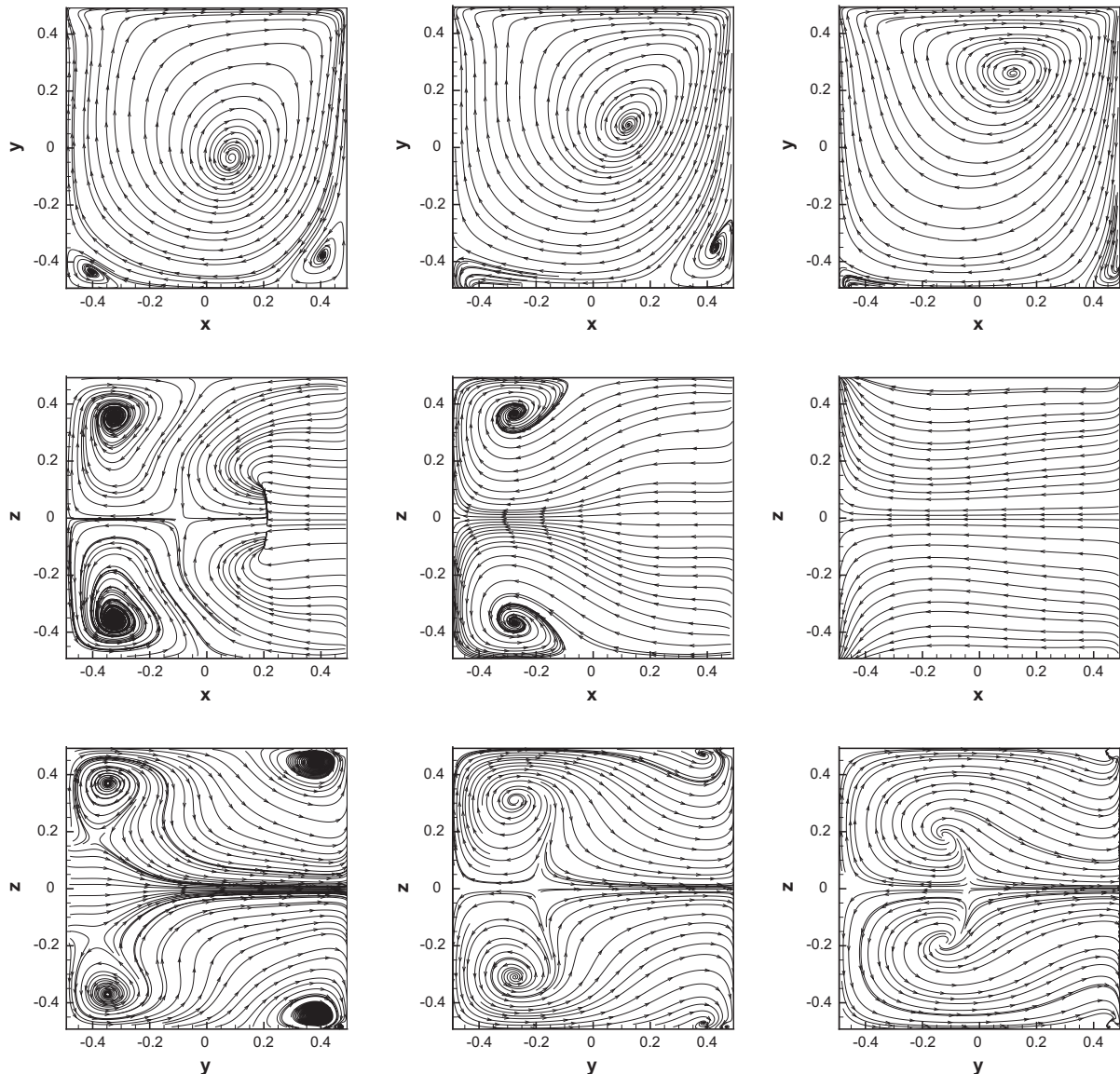

Fig. 9. 3D cavity flow: the streamline at $x-y$ plane with $z = 0$, $x-z$ plane with $y = 0$ and $y-z$ plane with $x = 0$ (from top to bottom) for $Re = 1000, 400$ and 100 (from left to right).

A non-equilibrium state inside the shock layer has been used for the flux evaluation with $\varepsilon = 0.1$ and $C = 3$ in (12). In the highly non-equilibrium region, the kinetic part in the gas distribution (7) plays a dominant role and the non-equilibrium state provides a physically consistent numerical dissipation. This is somehow consistent with the mechanism for the physical shock structure construction, in which the free transport and collision provides the mechanism for the shock formation.

4.4. Lid-driven cavity flow

The lid-driven cavity problem is one of the most important benchmarks for numerical Navier–Stokes solvers. In this case, the fluid is bounded by a unit cubic, driven by a uniform translation of the top boundary with $\gamma = 5/3$. Early three-dimensional cavity-flow calculations were carried out by De Vahl Davis and Mallinson [11] and Goda [17]. In this case, the flow is simulated
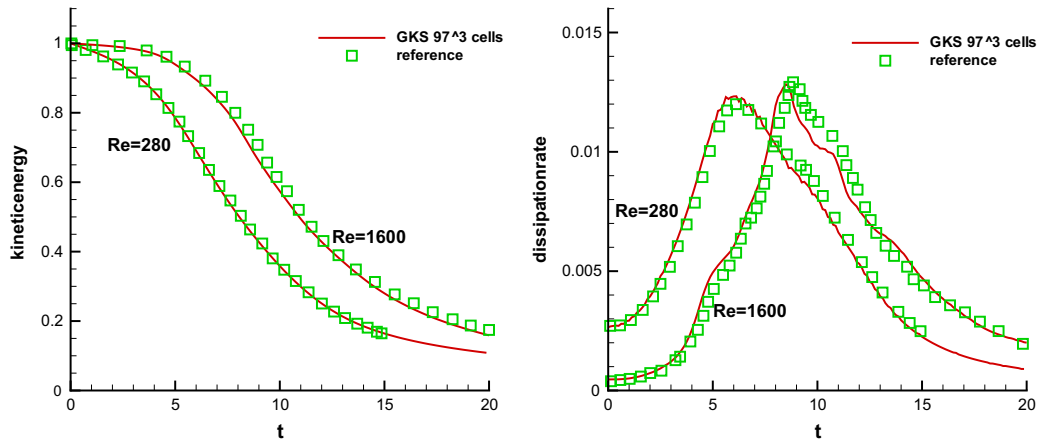
Fig. 10. Taylor–Green vortex problem: kinetic energy E_k (left) and dissipation rate $-dk/dt$ (right) using $97 \times 97 \times 97$ meshes points at the Reynolds numbers $Re = 1600$ and 280.
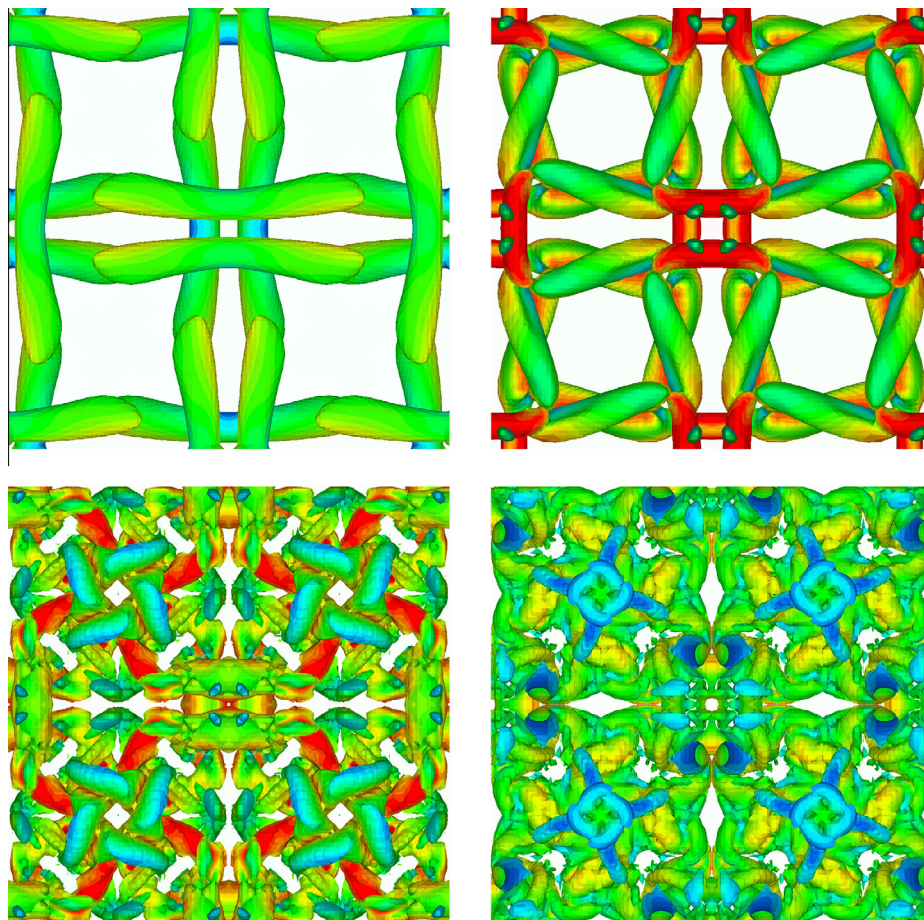
Fig. 11. Taylor–Green vortex problem: iso-surfaces of Q criterion colored by velocity magnitude at time $t = 2.5, 5, 8$ and 10 with $97 \times 97 \times 97$ mesh points at Reynold number $Re = 1600$. (For interpretation of the references to colour in this figure legend, the reader is referred to the web version of this article.)

with Mach number $Ma = 0.15$ and all the boundaries are isothermal and nonslip. Numerical simulations are conducted with three Reynolds numbers of $Re = 1000, 400$ and 100 using $65 \times 65 \times 65$ and $97 \times 97 \times 97$ mesh points for the domain $[-0.5, 0.5] \times [-0.5, 0.5] \times [-0.5, 0.5]$. The u-velocity profiles along the vertical centerline line, v-velocity profiles along the horizontal centerline in the $x–y$ plane with $z = 0$ and the benchmark data [1,34] are shown in Figs. 7 and 8. The simulation results match well with the benchmark data. The streamlines with $65 \times 65 \times 65$ mesh points at $x–y$ plane with $z = 0, x–z$ plane with $y = 0$ and $y–z$ plane with $x = 0$ for three different Reynolds numbers are presented in Fig. 9. This test shows that the high-order gas-kinetic scheme is effective to simulate complicated three-dimensional flow. The current accuracy can be hardly achieved from a high-order directional splitting method. With the directional splitting flux, the tangential derivatives of flow variables are not included in the flux function, and the vortex structure cannot be well resolved. As a reference, the CPU time for this case with $Re = 1000, 65 \times 65 \times 65$ mesh points, and running 100 time steps, is 315.364 s for the single machine with Intel Core i7-4770 CPU @ 3.40 GHz. Meanwhile, the CPU time for a 2D cavity flow with $Re = 1000, 65 \times 65$ mesh points, and running 100 time steps, is 1.985 s with the same machine.

4.5. Taylor–Green vortex

This problem is aimed at testing the performance of high-order methods on the direct numerical simulation of a three-dimensional periodic and transitional flow defined by a simple initial condition, i.e. the Taylor–Green vortex [3,12]. With a uniform temperature field, the initial flow field is given by

$$u = V_0 \sin\left(\frac{x}{L}\right) \cos\left(\frac{y}{L}\right) \cos\left(\frac{z}{L}\right),$$
$$v = -V_0 \cos\left(\frac{x}{L}\right) \sin\left(\frac{y}{L}\right) \cos\left(\frac{z}{L}\right),$$
$$w = 0,$$
$$p = p_0 + \frac{\rho_0 V_0^2}{16}\left(\cos\left(\frac{2x}{L}\right) + \cos\left(\frac{2y}{L}\right)\right)\left(\cos\left(\frac{2z}{L}\right) + 2\right).$$

The fluid is a perfect gas with $\gamma = 1.4$ and the Prandtl number is $Pr = 0.71$. Numerical simulations are conducted with two Reynolds numbers $Re = 1600$ and 280. The flow is computed within a periodic square box defined as $-\pi L \leqslant x, y, z \leqslant \pi L$. The characteristic convective time is $t_c = L/V_0$. In the computation, $L = 1$, $V_0 = 1, \rho_0 = 1$, and the Mach number takes $M_0 = V_0/c_0 = 0.1$, where c_0 is the sound speed.

The volume-averaged kinetic energy can be computed from the flow as it evolves in time, which is expressed as

$$E_k = \frac{1}{\rho_0 \Omega} \int_\Omega \frac{1}{2} \rho \mathbf{u} \cdot \mathbf{u} d\Omega,$$

where Ω is the volume of the computational domain, and the dissipation rate of the kinetic energy is given by

$$\varepsilon_k = -\frac{dE_k}{dt}.$$

To get a higher order accuracy, the fifth-order reconstruction is used for the conservative flow variables. The numerical results from the current scheme with $97 \times 97 \times 97$ mesh points are presented in Fig. 10 for the normalized volume-averaged kinetic energy and dissipation rate at Reynolds numbers $Re = 1600$ and 280, which agree well with the data in [6,12]. The iso-surfaces of Q criterions colored by velocity magnitude for Reynolds number $Re = 1600$ at $t = 2.5, 5, 8$ and 10 with $97 \times 97 \times 97$ mesh points

are shown in Fig. 11, which also agree well with the results in [3]. The evolution of flow structure from large vortices to more complex structures is evident.

5. Conclusion

In this paper, based on WENO reconstruction a high-order gas-kinetic scheme is proposed for three-dimensional Euler and Navier–Stokes solutions. Different from the traditional upwind and central schemes, the kinetic formulation is multidimensional, and inviscid and viscous terms coupling. More importantly, in the flux evaluation a multi-scale dynamic process from the kinetic to the hydrodynamic one is used [43], which provides a more consistent physical process for the gas evolution from a discontinuous initial condition than the well defined Euler and Navier–Stokes solutions. With the initial piece-wise polynomials of macroscopic flow variables, a time-dependent gas distribution function is obtained at the cell interface. With the space and time dependent gas distribution function, the flux transport along a cell interface within a time step can be integrated analytically. As a result, the Gaussian point integration and Runge–Kutta time stepping methods are not needed in the current scheme. The scheme has been tested from smooth flow to the flow with discontinuities, and the numerical results agree well with the exact solutions and benchmark data. These tests show that the high-order gas-kinetic scheme is effective to simulate complicated three-dimensional flows.

References

[1] Albensoeder S, Kuhlmann HC. Accurate three-dimensional lid-driven cavity flow. J Comput Phys 2005;206:536–58.
[2] Bhatnagar PL, Gross EP, Krook M. A model for collision processes in gases I: small amplitude processes in charged and neutral one-component systems. Phys Rev 1954;94:511–25.
[3] Bull JR, Jameson A. Simulation of the compressible Taylor–Green vortex using high-order flux reconstruction schemes. AIAA 2014-3210.
[4] Cercignani C. The Boltzmann equation and its applications. Springer-Verlag; 1988.
[5] Chapman S, Cowling TG. The mathematical theory of non-uniform gases. 3rd ed. Cambridge University Press; 1990.
[6] Chapelier J, Plata MDLL, Renac F, Martin E. Final abstract for ONERA Taylor–Green DG participation. In: 1st International workshop on high-order CFD methods, at the 50th AIAA aerospace sciences meeting Nashville, TN; January 2012.
[7] Cockburn B, Shu CW. TVB Runge–Kutta local projection discontinuous Galerkin finite element method for conservation laws II: general framework. Math Comput 1989;52:411–35.
[8] Cockburn B, Shu CW. The Runge–Kutta discontinuous Galerkin method for conservation laws V: multidimensional systems. J Comput Phys 1998; 141:199–224.
[9] Cockburn B, Shu CW. The local discontinuous Galerkin method for time-dependent convection–diffusion systems. SIAM J Numer Anal 1998; 35:2440–63.
[10] Daru V, Tenaud C. High order one-step monotonicity-preserving schemes for unsteady compressible flow calculations. J Comput Phys 2004;193:563–94.
[11] De Vahl Davis G, Mallinson GD. An evaluation of upwind and central difference approximations by a study of recirculating flow. Comp Fluids 1976;4:29–43.
[12] Debonis J. Solutions of the Taylor–Green vortex problem using high-resolution explicit finite difference methods. AIAA paper 2013-0382; 2013.
[13] Dumbser M, Balsara DS, Toro EF, Munz CD. A unified framework for the construction of one-step finite volume and discontinuous Galerkin schemes on unstructured meshes. J Comput Phys 2008;227:8209–53.
[14] Dumbser M. Arbitrary high order $P_N P_M$ schemes on unstructured meshes for the compressible Navier–Stokes equations. Comput Fluids 2010;39:60–76.

[15] Dumbsera M, Käser M, Titarevb VA, Toro EF. Quadrature-free non-oscillatory finite volume schemes on unstructured meshes for nonlinear hyperbolic systems. J Comput Phys 2007;226:204–43.

[16] Gao H, Wang ZJ. A high-order lifting collocation penalty formulation for the Navier–Stokes equations on 2D mixed grids. AIAA paper 2009 3784.

[17] Goda K. A multistep technique with implicit difference schemes for calculating two- or three-dimensional compressible cavity flows. J Comput Phys 1979;30:76–95.

[18] Harten A, Engquist B, Osher S, Chakravarthy SR. Uniformly high order accurate essentially non-oscillatory schemes, III. J Comput Phys 1987;71:231–303.

[19] Huynh HT. A flux reconstruction approach to high-order schemes including discontinuous Galerkin methods. AIAA paper 2007 4079.

[20] Huynh HT. A reconstruction approach to high-order schemes including discontinuous Galerkin for diffusion. AIAA paper 2009 403.

[21] Hu C, Shu CW. Weighted essentially non-oscillatory schemes on triangular meshes. J Comput Phys 1999;150:97–127.

[22] Jiang GS, Shu CW. Efficient implementation of weighted ENO schemes. J Comput Phys 1996;126:202–28.

[23] Kim KH, Kim C. Accurate, efficient and monotonic numerical methods for multi-dimensional compressible flows Part I: spatial discretization. J Comput Phys 2005;208:527–69.

[24] Li Q, Xu K, Fu S. A high-order gas-kinetic Navier–Stokes flow solver. J Comput Phys 2010;229:6715–31.

[25] Liu XD, Osher S, Chan T. Weighted essentially non-oscillatory schemes. J Comput Phys 1994;115:200–12.

[26] Liu Y, Vinokur M, Wang ZJ. Spectral difference method for unstructured grids I: basic formulation. J Comput Phys 2006;216:780–801.

[27] Luo H, Luo L, Nourgaliev R, Mousseau VA, Dinh N. A reconstructed discontinuous Galerkin method for the compressible Navier–Stokes equations on arbitrary grids. J Comput Phys 2010;229:6961–78.

[28] Luo J, Xu K. A high-order multidimensional gas-kinetic scheme for hydrodynamic equations. Sci China Technol Sci 2013;56:2370–84.

[29] Mieussens L. On the asymptotic preserving property of the unified gas-kinetic scheme for the diffusion limit of linear kinetic models. J Comput Phys 2013;253:138–56.

[30] Pan L, Xu K. Generalized coordinate transformation and gas-kinetic scheme. J Comput Phys 2015;287:207–25.

[31] Pandolfi M, D'Ambrosio D. Numerical instabilities in upwind methods: analysis and cures for the carbuncle phenomenon. J Comput Phys 2001;166:271–301.

[32] Reed WH, Hill TR. Triangular mesh methods for the neutron transport equation. Technical report LA-UR-73-479, Los Alamos Scientific Laboratory, Los Alamos; 1973.

[33] Sjögreen B, Yee HC. Grid convergence of high order methods for multiscale complex unsteady viscous compressible flows. J Comput Phys 2003;185:1–26.

[34] Shu C, Wang L, Chew YT. Numerical computation of three-dimensional incompressible Navier–Stokes equations in primitive variable form by DQ method. Int J Numer Meth Fluids 2003;43:345–68.

[35] Shu CW. Essentially non-oscillatory and weighted essentially non-oscillatory schemes for hyperbolic conservation laws. Lecture notes in mathematics. Springer; 1998.

[36] Shu CW, Osher S. Efficient implementation of essentially non-oscillatory shock capturing schemes. J Comput Phys 1988;77:439–71.

[37] Titarev VA, Toro EF. Finite-volume WENO schemes for three-dimensional conservation laws. J Comput Phys 2004;201:238–60.

[38] Titarev VA, Toro EF. ADER schemes for three-dimensional nonlinear hyperbolic systems. J Comput Phys 2005;204:715–36.

[39] Wang ZJ. Spectral (finite) volume method for conservation laws on unstructured grids: basic formulation. J Comput Phys 2002;178:210–51.

[40] Wang ZJ, Gao H. A unifying lifting collocation penalty formulation including the discontinuous Galerkin, spectral volume/difference methods for conservation laws on mixed grids. J Comput Phys 2009;228:8161–86.

[41] Xu K. Gas kinetic schemes for unsteady compressible flow simulations. Lecture note Ser. 1998-03, Von Karman Institute for fluid dynamics lecture; 1998.

[42] Xu K. A gas-kinetic BGK scheme for the Navier–Stokes equations and its connection with artificial dissipation and Godunov method. J Comput Phys 2001;171:289–335.

[43] Xu K. Direct modeling for computational fluid dynamics, construction and application of unified gas-kinetic schemes. World Scientific; 2015.

[44] Xu K, Huang J. A unified gas-kinetic scheme for continuum and rarefied flows. J Comput Phys 2010;229:7747–64.